RESEARCH ARTICLE

Antheraea pernyi silk fibroin bioinks for digital light processing 3D printing

Xue Zhang[†], Wenbi Wu[†], Yulan Huang, Xiong Yang, Maling Gou*

State Key Laboratory of Biotherapy West China Hospital, Sichuan University, Chengdu, Sichuan, China

(This article belongs to the *Special Issue: 3D Bioprinting with Photocurable Bioinks*)

Abstract

The application of three-dimensional (3D) bioprinting has increased in the biomedical field. The lack of bioinks with both biocompatibility and printability is still a problem to be solved. Silk fibroin materials have good biocompatibility and have a broad application prospect in the field of biomedical materials. At present, most research usually involves *Bombyx mori* silk fibroin (BSF). However, BSF has low cell adhesion. Compared with BSF, *Antheraea pernyi* silk fibroin (ASF) isolated from typical non-mulberry silk exhibits a unique arginine-glycine-aspartate (RGD) sequence with good cell adhesion enhancement. In this study, we developed a bioink based on ASF for digital light processing (DLP) 3D bioprinting. The ASF-based bioinks (ASF-MA) were produced by a methacryloylation process using methacrylic anhydride (MA) to achieve the properties of photopolymerization reaction. The ASF-MA hydrogel has mechanical properties, biocompatibility, and especially cell adhesion. Meanwhile, we found that the ASF-MA hydrogels promoted the adhesion, migration, and proliferation of S16 cells. Hence, the ASF-MA hydrogels had the potential applications in biomedical fields.

Keywords: *Antheraea pernyi* silk fibroin; Hydrogels; Photopolymerization; Mechanical properties; Bioprinting

[†]These authors contributed equally to this work.

*Corresponding author:
Maling Gou
(goumaling@scu.edu.cn)

1. Introduction

Three-dimensional (3D) printing technology was a subversive technology emerging in recent years. It has unique advantages in personalized and complex structure manufacturing. Despite the increasing application of 3D bioprinting in the biomedical field, there was still a lack of bioinks with good biocompatibility and printability. At present, the biomaterials used for bioinks were mainly natural or synthetic polymers because of their biocompatibility and printability. Natural polymers were one of the more desired biomaterials since they were more immune system-friendly, cheaper, easier to obtain, and more biodegradable than synthetic polymers[1-4]. Currently, the most commonly used photopolymerized printing inks were protein, polysaccharide, and synthetic biomaterials, and most of them were modified chemically with photoreactive functional groups, such as gelatin-methacryloyl (GelMA), *Bombyx mori* silk fibroin-glycidyl methacrylate (BSF-GMA), thiol-ene gelatin, methacrylate-based hyaluronic acid, sodium alginate, and polyethylene glycol diacrylate (PEGDA)[5,6]. Silk fibroin is a type of protein extracted mostly from silkworms that is one of the

natural polymer-based biomaterials. It not only meets the basic requirements for biomaterials but also has great mechanical properties. Thus, silk fibroin becomes a good choice for the creation of biomaterials[7-10]. Compared with the mulberry silkworms, which fed on mulberry leaves, the non-mulberry silkworms are mostly free-ranging in the wild and consume different types of food. The typical representatives are *Antheraea pernyi* in China, *Antheraea yamamai* in Japan, *Antheraea mylita*, *Antheraea assamensis,* and *Philosamia ricini* in India, as well as other varieties. The common non-mulberry silk fibroin has some unique amino acid sequences in its molecular chain, which are expected to give non-mulberry silk fibroin-based biomaterials more widespread properties and make them promising for biomedical applications, especially in fields related to cell culture and tissue regeneration[11-14].

Antheraea pernyi silk fibroin (ASF), a non-mulberry silk fibroin with good mechanical properties and stability, can be obtained from a wild non-mulberry silkworm by extracting the silk glue. ASF is composed of alanine (43.07%), glycine (27.27%), serine (11.26%), tyrosine (5.26%), and aspartate (4.47%)[15-17]. Compared with *Bombyx mori* silk fibroin (BSF), ASF contains a certain amount of unique arginine-glycine-aspartic acid (RGD) tripeptide sequence. The RGD sequence was the binding site for cellular integrin receptors which could effectively promote the adhesion of cells to biomaterials[18,19]. Due to its good biocompatibility and mechanical properties, ASF has been used in wound dressings, drug delivery carriers, and tissue engineering scaffold materials in recent years[20]. As demonstrated in a study, ASF nanoparticles were loaded with differently charged small-molecule drugs, such as doxorubicin hydrochloride, ibuprofen, and ibuprofen-Na, through electrostatic interactions, to achieve slow drug release[21]. Cui *et al.* prepared a composite scaffold with skin affinity as well as good air and water permeability by mixing collagen and ASF. The scaffold had the potential to improve wound healing when loaded with bone mesenchymal stem cells, providing a new option for skin tissue engineering[22]. Zou *et al.* prepared the ASF scaffold by using the freeze-drying method. The ASF scaffold could promote the viability, cytocompatibility, and migration ability of Schwann cells and might have great potential applications in the area of nerve tissue engineering[23]. ASF is a great biomaterial with many advantages in biomedical applications. Nevertheless, ASF has not been used in photocurable 3D printing due to the lack of crosslinking sites for photopolymerization.

In our study, by reacting methacrylic anhydride (MA) with the amino groups of ASF, we prepared an ASF-based bioinks (ASF-MA) for digital light processing (DLP) 3D printing (Scheme 1A). We evaluated the effect of ASF methacryloylation degree on protein structure and hydrogel mechanical properties. We used ethanol solvent soaking method to enhance the mechanical properties of ASF-MA hydrogels with different concentrations. In addition, we theoretically analyzed the possible reasons for the enhanced mechanical properties based on the results of secondary structure and surface morphology. Afterward, we demonstrated the printability of the ASF-MA bioink using a DLP 3D printer (Scheme 1B). We investigated the biocompatibility and degradability of ASF-MA bioink *in vivo* and *in vitro*. Lastly, we discovered that ASF-MA hydrogel can promote the adhesion, migration, and myelination of S16 cells through a comparison with different hydrogels. In this study, we preliminarily explored the potential use of ASF-MA as a scaffold material for peripheral nerve defect repair.

ASF-MA bioink is a new material candidate for light-curing 3D printing technologies such as DLP.

2. Materials and methods

2.1. Materials
Wild *Antheraea pernyi* silkworm cocoons were purchased from Nanyang, Henan Province. *Bombyx mori* silkworm cocoons were purchased from Jiangnan Cocoon and Mulberry Base (Jiaxing, Zhejiang). Gelatin and methacrylic anhydride were purchased from Sigma-Aldrich. Glycidyl methacrylate (GMA) was purchased from Adamas. Na_2CO_3 was purchased from Tianjin Bodi Chemical Co., Ltd. $Ca(NO_3)_2 \cdot 4H_2O$ was purchased from Tianjin Damao Chemical Reagent Factory. All chemical reagents are of analytical grade. Rat Schwann cells (S16) and human umbilical vein endothelial cells (HUVECs) were purchased from Beijing Beina Chuanglian Biotechnology Research Institute. The mouse embryonic fibroblast cell line (NIH/3T3) and the red fluorescent protein-labeled mouse colon cancer cell line (CT26-RFP) were purchased from the American Type Culture Collection (ATCC). Green fluorescent protein (GFP)-labeled mouse bone marrow stromal cells (OP9-GFP) were provided by other research groups. BALB/c male mice were purchased from Chengdu Dashuo Experimental Animal Co., Ltd.

2.2. Preparation of hydrogels

2.2.1. Extraction of Antheraea pernyi silk fibroins
According to the method reported in the literature[24], the extraction method was slightly optimized and improved in this study. Specifically, the empty *Antheraea pernyi* silkworm cocoons were washed with water to remove dirt, dried, and then cut into four or five pieces. Forty grams of *Antheraea pernyi* silkworm cocoons were degummed
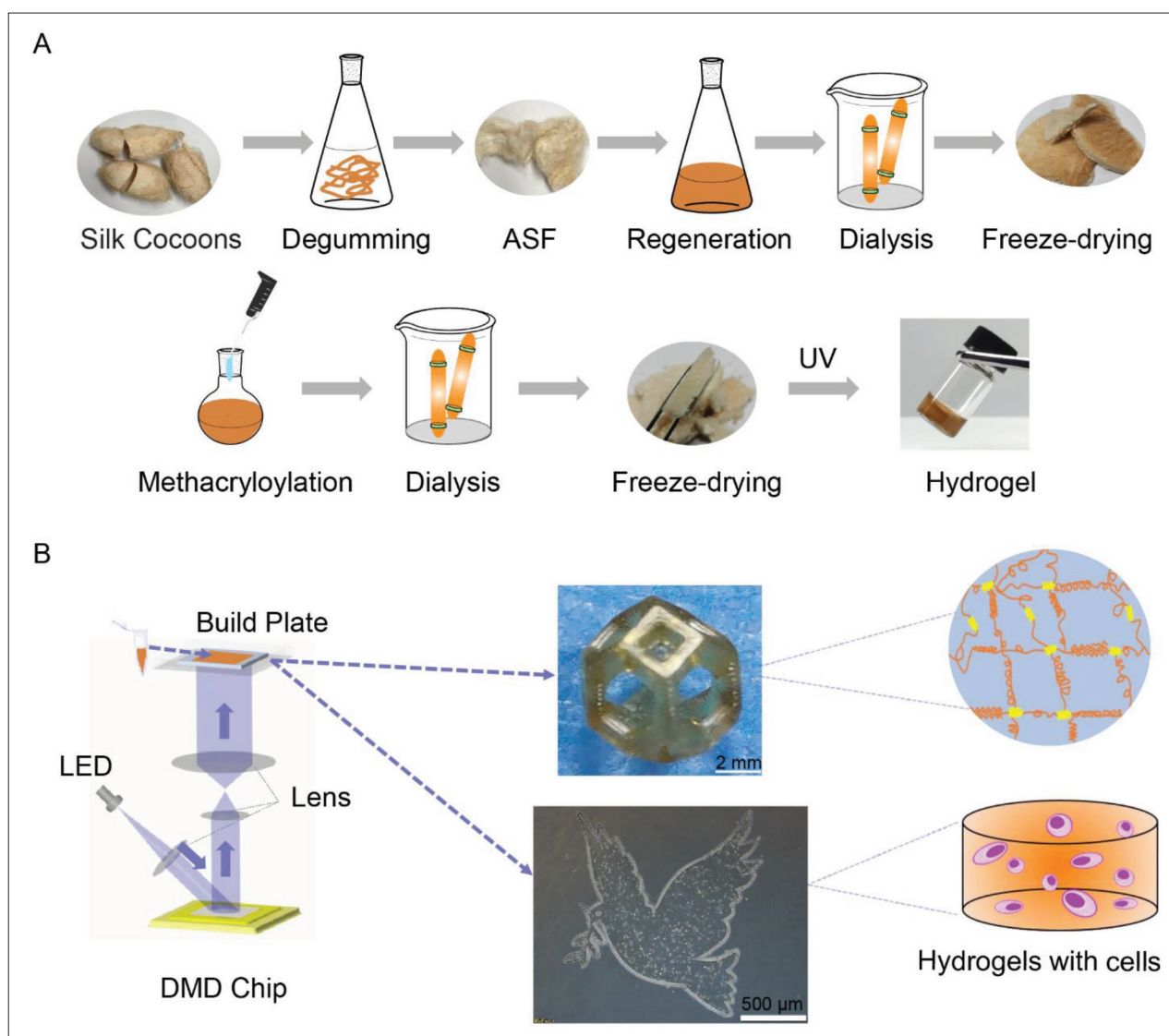
Scheme 1. Schematic presentation for methacryloylation of *Antheraea pernyi* silk fibroin with methacrylic anhydride (MA) (ASF-MA) and bioprinting of cells with ASF-MA by digital light processing (DLP) 3D printer. (A) Preparation process of ASF-MA hydrogels. (B) The diagram of continuous DLP 3D printing and 3D-printed structure. Abbreviations: DMD, digital micromirror device; LED, light-emitting diode; UV, ultraviolet.

with 1 L of 0.05 M Na_2CO_3 solution at 100°C for 15 min for three times. After the sericin was removed, the ASF was washed several times with distilled water and wrung dry. Until there was no turbid residue in the water, the ASF were dried at room temperature.

2.2.2. Regeneration of Antheraea pernyi silk fibroins
Five hundred grams of $Ca(NO_3)_2 \cdot 4H_2O$ were placed in a 500-mL round-bottomed flask, heated and melted at 105°C in an oil bath, and slowly added with 25 g of *Antheraea pernyi* silk fibroins. The solution was dark brown and was stirred continuously to dissolve *Antheraea pernyi* silk fibroins. After 4 h, the solution was dialyzed against distilled water using 3500-kDa cutoff dialysis bags at

4°C for 3 days, and freeze-dried to obtain about 20 g of regenerated *Antheraea pernyi* silk fibroins, which were soft light-brown solid.

2.2.3. Preparation of ASF-MA hydrogels
To ensure the stability of the methacryloylated ASF, 1 g of the regenerated ASF was dissolved in 10 mL of the prepared 0.25 M carbonate buffer (CB) solution and stirred in an ice bath. Then, 10, 25, 50, 100, and 150 μL of MA were slowly added and reacted for 6 h, denoted as ASF-MA$_{1\%}$, ASF-MA$_{2.5\%}$, ASF-MA$_{5\%}$, ASF-MA$_{10\%}$, and ASF-MA$_{15\%}$, respectively. The prepared solution was filtered and dialyzed at 4°C for 7 days. ASF-MA solutions were frozen at -80°C and freeze-dried.

2.2.4. Preparation of ASF-MA hydrogels

ASF-MA was dissolved in water or phosphate-buffered saline (PBS) at 10%, 20%, and 30% w/v concentrations. Lithium phenyl-2,4,6-trimethylbenzoylphosphinate (LAP, 1 wt%) was added and mixed until it was fully dissolved. The bioinks were exposed to the DLP 3D printer with an exposure intensity of 80 mW/cm^2 for 5 s to form ASF-MA hydrogels, which were denoted as 10% ASF-MA$_{2.5\%}$, 20% ASF-MA$_{2.5\%}$, 30% ASF-MA$_{2.5\%}$, 10% ASF-MA$_{5\%}$, 20% ASF-MA$_{5\%}$, 30% ASF-MA$_{5\%}$, 10% ASF-MA$_{10\%}$, 20% ASF-MA$_{10\%}$, and 30% ASF-MA$_{10\%}$. The above-mentioned formed hydrogels were soaked in 75% ethanol solution, water, and PBS for 4 h to obtain ASF-MA EtOH, ASF-MA H$_2$O, and ASF-MA PBS.

2.2.5. Preparation of other hydrogels

GelMA and BSF-GMA were synthesized according to the previously reported method[25]. Then, a certain amount of GelMA or BSF-MA were dissolved, and 1 wt% LAP was added to water or PBS to prepare 20% w/v bioinks. The bioinks were exposed to a DLP 3D printer with an exposure intensity of 80 mW/cm^2 for 5 s to obtain GelMA or BSF-MA hydrogel.

2.3. Characterization

Proton nuclear magnetic resonance (^{1}H-NMR) spectra were recorded by using a Bruker 400-MHz spectrometer. Scanning electron microscopy (SEM) was performed on a JSM-7500F electron microscope operating at 30 kV. Fourier transform infrared (FTIR) spectra were recorded on a Nicolet 6700 spectrophotometer. To quantify the composition of the secondary structure, Peakfit 4.12 software (SeaSolve software, USA) was used to analyze the second derivative of the spectrum amide I region (1580–1710 cm^{-1}). Sub-peak structures refer to the wavelength range described by Nucara *et al.*[23,26,27].

2.4. Determination of methacryloylation degree

Trinitrobenzene sulfonic acid (TNBS) assay was carried out to determine the degree of substitution of amino groups in ASF-MA[28]. Briefly, ASF and ASF-MA samples were dissolved in 0.1 M sodium bicarbonate buffer at 1.6 mg/mL, respectively. Each sample was combined with 0.5 mL of 0.01% TNBS solution for 3 h. Approximately 0.25 mL 1 M HCl and 0.5 mL 10% w/v sodium dodecyl sulfate were added to stop the reaction. The absorbance of the sample at 335 nm was measured. Then, a standard curve of glycine was simulated to determine the amino concentration, where sample solutions were prepared as 0, 8, 16, 32, and 64 µg/mL.

2.5. Mechanical property measurement

Compression and tensile tests were performed on DMA Q800 dynamic mechanics analyzer. The cylindrical shape hydrogel samples were used for the uniaxial compression measurements. ASF-MA PBS samples were compressed to the bottom at a speed of 1 mm min^{-1}, and ASF-MA EtOH samples were compressed at speed of 2 mm min^{-1}. The compression test could not be performed because the 10% ASF-MA$_{2.5\%}$ hydrogel was too soft and brittle. The cuboid hydrogel samples were used for the uniaxial tensile measurements, and the tensile rate was 10 mm min^{-1}. Only ASF-MA EtOH samples were subjected to tensile test, because they were too brittle without ethanol immersion. At least three samples from each group were tested.

2.6. *In vitro* degradation test

ASF-MA$_{10\%}$ hydrogels were prepared for degradation study following the previously described protocol[29,30]. *In vitro* degradation analysis was carried out in PBS (pH 7.4) and freshly prepared protease XIV (Sigma-Aldrich, USA) at 37°C on a 24-well plate with 0.05% sodium azide. The initial weight of hydrogels was measured using an electronic balance. Samples were replenished with fresh protease solution after every 72 h. The control samples were kept in 1× PBS (control) with 0.05% sodium azide. At pre-determined time points, the ASF-MA hydrogels were washed with water and wiped with tissue paper to remove excess water and then weighed.

$$\text{Percent mass remaining} = (Mt/Mi) \times 100\% \qquad \text{(I)}$$

Mt is weight at a predetermined time point, and Mi is initial weight.

2.7. 3D printing

To enhance the accuracy of the 3D printing structure, ASF-MA$_{10\%}$ with the highest degree of methacryloylation was selected as the ink for test printing. The appropriate concentration was selected as 20 wt%. The LAP concentration was 1 wt%. The principle of continuous DLP 3D printing technology is illustrated in Scheme 1B. The designed structures were sliced into a series of images, which were projected into the test inks for polymerization by a digital micromirror device. Moreover, 0.1% lemon yellow was added to the solution to reduce the interference of excess light in the bioinks. The obtained hydrogel structures were immersed in PBS to remove the LAP, lemon yellow, and uncrosslinked polymers.

2.8. 3D bioprinting

To test the 3D bioprintability of ASF-MA bioinks, we decided to mix fluorescent cells with ASF-MA bioinks to print a flat pattern, observed the cell state, and recorded the cell fluorescence intensity. First, we designed a printable two-dimensional image based on the "Yin-Yang Tai Chi" diagram and the "peace dove." Then, we uploaded the two-dimensional images to the PRO 4500 projection device of the DLP 3D

Table 1. Primers used in RT-PCR

Gene name	Forward primer sequence (5' to 3')	Reverse primer sequence (5' to 3')
NCAD	CACCCGGCTTAAGGGTGATT	CGATCCTGTCTACGTCGGTG
NCAN	GTGAAGTCAGCCATCCACCA	TCGGGACGAGTGTAGAGTGT
Integrin β1	ACTCAGTGAACAGCAACGGTGAAG	TCCAAATCAGCAGCAAGGCAAGG
Cdc42	GCTGTCAAGTATGTGGAGTGT	GGCTCTGGAGATGCGTTCA
Rac1	CAATGCGTTCCCTGGAGAGT	AACACGTCTGTTTGCGGGTA
MPZ	CTGCCCTGCTCTTCTCTTCTTTGG	GAGCCCACAGCACCATAGACTTC
PMP22	GGTGCTAGTGTTGCTCTTCGTCTC	CAAGGCGGATGTGGTACAGTTCTG
GAPDH	AACTTTGGCATCGTGGAAGG	TGGATGCAGGGATGATGTTCTG

printing system. We set the experimental parameters as follows: the exposure intensity was 80 mW/cm^2, the exposure time was 5 s, and the thickness was 0.1 mm. We selected ASF-MA$_{10\%}$ with the highest degree of methacryloylation; the appropriate concentration was 20 wt%; the LAP concentration was 1 wt%. To print the "peace dove," we mixed the ASF-MA bioinks with the red fluorescent protein-labeled mouse colon cancer cells (CT26-RFP). We placed the bioinks with cells on a circular slide with a diameter of 16 mm for bioprinting. Similarly, to print the "Yin-Yang Tai Chi" diagram, we mixed the ASF-MA bioinks with CT26-RFP cells and GFP-labeled mouse bone marrow stromal cells (OP9-GFP), respectively, and printed it twice. We placed the bioinks with cells on a circular slide with a diameter of 16 mm for bioprinting. We used sterile PBS to wash to remove uncrosslinked monomers and other impurities. Then, we continued to print on the slide for the second time. After printing, we transferred the sample to the 12-well plate. We used sterile PBS to wash 6 times for 5 min each time. After 15 min, we replaced PBS with Dulbecco's Modified Eagle Medium. We placed the 12-well plate in incubator. Finally, on the 1, 2, and 3 days, we observed the cell state and recorded the fluorescence intensity under the fluorescence microscope.

2.9. Cytocompatibility of hydrogel

ASF-MA$_{10\%}$ (20 wt%) was used for the printing bioinks. S16 cells, NIH/3T3 cells, and HUVECs in the logarithmic growth phase were inoculated at a density of 8×10^2 cells/well, 1×10^3 cells/well, and 1×10^3 cells/well in the 96-well plate, respectively. After 1, 3, 5, and 7 days of culture, the cell growth and proliferation on the hydrogels were assessed by using CCK-8 assay according to the protocol. The S16 cells, NIH/3T3 cells, and HUVECs in the logarithmic growth phase were respectively seeded onto the printed hydrogel in a 12-well plate at a density of 2×10^4 cells/well and cultured in an incubator. After 1, 3, and 5 days of incubation, live/dead assays were employed to examine the viability, and the cells were photographed under a fluorescence microscope.

2.10. Immunofluorescence staining

Cells were inoculated on the samples and cultured as described above. After 48 h, the samples were fixed in 4% paraformaldehyde in PBS and permeabilized with 0.5% Triton X-100 for 20 min. The samples were then blocked with normal goat serum for 30 min for non-specific binding. The rabbit adherent spot protein antibody (1:100) was incubated overnight at 4°C. The next day, Alexa Fluor® 488-labeled goat anti-rabbit IgG (1:50), rhodamine ghost pen cyclic peptide (1:50), and DAPI PBS solution were added and incubated at room temperature, and all mounted samples were visualized by confocal laser scanning microscopy.

2.11. RNA isolation and real-time reverse transcription-polymerase chain reaction

The mRNA expression levels of related genes including NACD, Integrin β1, Cdc42, Rac1, MPZ, and PMP22 were examined using real-time reverse transcription-polymerase chain reaction (RT-PCR), and glycerol triphosphate dehydrogenase (GAPDH) was selected as the housekeeping gene. RT-PCR procedure was performed as follow: First, cellular RNA was extracted using a total RNA extraction kit. The RNA concentration of each group was measured using a nucleic acid and protein analyzer, and the RNA was stored in a -80°C freezer. Next, reverse transcription was performed using the extracted RNA as template RNA. The reverse transcription reaction was performed in a PCR machine. The cDNA was obtained after the reaction and stored in a -20°C refrigerator for subsequent experiments. Finally, using GAPDH as an internal reference, the mRNA expression levels of NCAD, Integrin β1, Cdc42, Rac1, MPZ, and PMP22 were analyzed by RT-PCR. All primers used are listed in Table 1.

2.12. *In vivo* degradation test and histological evaluation

Cylindrical hydrogels (6 mm diameter, 2 mm height) were fabricated from sterile ASF-MA$_{10\%}$, GelMA, and BSF-GMA printing inks by 3D printing. We used SPF-grade BALB/c male mice for dorsal subcutaneous implantation
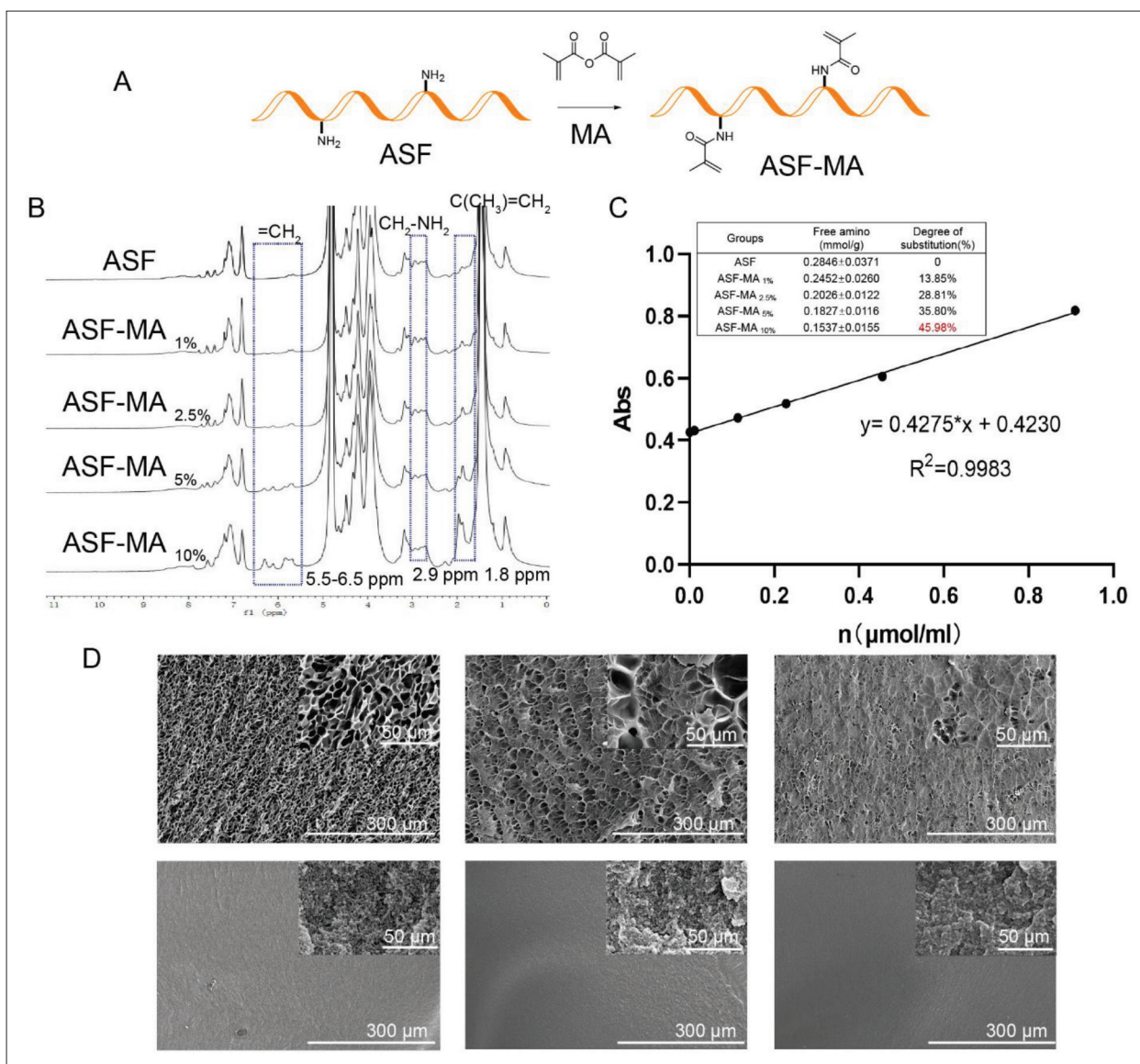
Figure 1. (A) The synthetic route of ASF-MA. (B) The ^{1}H-NMR spectra of ASF and ASF-MA. (C) Standard curve and the content of free amino groups of ASF-MA. (D) The SEM images of the different ASF-MA hydrogels.

experiments. First, mice were anesthetized using approved procedure. The back of the mouse was shaved and disinfected. Three wounds of 2 cm were cut on the back skin with sterilized surgical instruments, and the skin was partially separated. ASF-MA$_{10\%}$, GelMA, and BSF-GMA hydrogels were implanted subcutaneously on the back. The back skin of the mouse was sutured with 8-0 sutures. The mice were euthanized at pre-determined time points (1, 2, 3, 4, 8, 10, and 12 weeks) after transplantation to harvest the transplanted hydrogels together with the surrounding tissues. We weighed the transplanted hydrogel after removing the outer fibrous capsule and surface liquid for record. The degradation rate was shown as the ratio of wet weight to initial wet weight at each time point.

2.13. Statistical analysis

Three independent experiments with three parallel samples per experiment were undertaken, unless otherwise stated. The data are expressed as mean ± standard deviation (SD). The statistical difference was analyzed by one-way analysis of variance (ANOVA) using the GraphPad Prism software (*ns*: $p > 0.05$, *$p < 0.05$, **$p < 0.01$, ***$p < 0.001$).

3. Results

3.1. Characteristics of ASF-MA

The ASF-MA bioink was prepared by reacting MA with free amino groups on ASF (Figure 1A). While preparing ASF-MA, ASF would coagulate and could not be reconstituted

when MA exceeded 150 μL. The main reason for this phenomenon was that both ASF and MA are hydrophobic. The excessive addition of MA would lead to an increase in molecular weight and coagulation. To find the appropriate amount of MA, ASF-MA was manufactured by adding 10, 25, 50, and 100 μL MA separately to the ASF solution. The properties of ASF-MA hydrogels were related to the amount of MA. The nucleophilic addition reactions of MA to the primary amine of lysine in ASF described above were confirmed by ^{1}H-NMR (Figure 1B). We found that the characteristic resonances within the methacrylamide vinyl group (δ = 5.5–6.5 ppm) and the methyl group (δ = 1.8 ppm) of MA appeared by adding MA. In addition, the lysine methylene signal (δ = 2.9 ppm) at the MA gradually decreased as the MA volume increased, which substantiated the modification of lysine residues in the ASF by MA. The results of the TNBS assay are shown in Figure 1C. According to the calculated results, 1 g of ASF contained about 0.28 mmol of free amino groups. The degree of substitution was 13.85%, 28.81%, 35.80%, and 45.98% with 10, 25, 50, and 100 μL added MA, respectively. We proved that the methacryloyl content of the ASF molecular chain increased with the addition of MA.

We used SEM to observe the internal structure of the hydrogel (Figure 1D) for ASF-MA H_2O hydrogels immersed in water that was formulated by the liquid nitrogen fast freezing method. As the concentration increased, the cross-section of the hydrogel became denser. The pore diameter of 10% hydrogel was about 15.15 ± 2.10 μm. Compared with 10% hydrogel, 20% hydrogel showed smaller nanopores. The pore diameter of 20% hydrogel was about 6.18 ± 3.30 μm, and the difference of the 20% hydrogel was relatively significant. We observed that part of them were at the nanometer level, while the rest of them were large. The 30% of ASF-MA hydrogel had pore size measured in nanometers. ASF-MA EtOH hydrogels were prepared by the critical point drying method. The pore size was significantly different from the liquid nitrogen freeze-dried samples, and most of them were dense nanopores. The cross-section of the material became denser with increasing concentration of ASF-MA. The method of soaking in alcohol also made the hydrogel structure denser.

3.2. Physical properties of ASF-MA
We further performed a detailed FTIR data analysis to characterize the chemical modification of ASF by MA and found that the secondary structure of proteins was affected by various factors. Moreover, the secondary structure of the protein was related to the mechanical properties of the hydrogel. There were three main characteristic areas of protein in the infrared spectrum, which were the amide I band (1600–1700 cm^{-1}), amide II band (1480–1575 cm^{-1}),

and amide III band (1220–1330 cm^{-1}). In Figure 2A, it showed that both gel photocuring process and ethanol soaking process could significantly alter the bands of amides I, II, and III.

To analyze the secondary structural fraction of materials, we used the Peakfit v4.12 software[31] for multi-peak separations which contained four types of common proteins in secondary structure. They were β-sheet (1615–1640 cm^{-1}, 1680–1690 cm^{-1}), β-turn (1660–1680 cm^{-1}), random coil (1640–1650 cm^{-1}), and α-helix (1650–1660 cm^{-1}). In the amide I region (1600–1700 cm^{-1}), it was mainly the stretching vibration of the carbonyl group (C=O), which was sensitive to the change of the secondary structure. The amide I band was quantified by using the second derivative of a Gaussian function fit (Figure 2B). The relative content of each secondary structure was calculated according to the peak area of each fitting curve (Figure 2C). The content of MA had a specific influence on the secondary structure level of ASF. As the MA content increased, the β-sheet decreased from 25 ± 0.79% to 19.5 ± 0.78%. Meanwhile, the α-helix and random coil increased slightly from 59.07 ± 0.72% to 66.8 ± 0.96%, while the β-turn angle did not change significantly. The β-sheet percentage increased significantly to 26.6 ± 0.63%, after ASF-MA10% hydrogel formed by photopolymerization was lyophilized. The β-sheet percentage increased significantly to 26.6 ± 0.63%, after ASF-MA10% hydrogel formed by photopolymerization was lyophilized. After soaking the hydrogel in 75% ethanol for 4 h, the β-fold content dramatically rose to 65.5 ± 0.60%, which was about 1.5 times more than the β-fold content of the unprocessed hydrogel. At the same time, the total amounts of α-helix and random coil dropped drastically to 26.39 ± 0.60%. The proportions of both α-helix and random coil showed decreasing trends, especially the quantity of the random coil which showed a reduction from 43.3 ± 1.20% to 13.4 ± 0.81%. In summary, the modification of MA could affect the secondary structure of ASF. Still, the photopolymerization and ethanol immersion had a greater effect on it and resulted in a significant increase in the β-sheet and crystalline state fraction.

Then, the compressive properties of hydrogels with different concentrations and degrees of substitution were measured. As shown in Figure 2D, the compressive properties of the ASF-MA PBS hydrogels enhanced with the degree of methacryloylation and concentration. The compressive strength of 30% ASF-MA$_{10\%}$ PBS could reach 269 kPa (35% deformation). However, 10% ASF-MA$_{10\%}$ PBS and 30% ASF-MA$_{2.5\%}$ PBS under the same deformation were only 5.6 and 15.1 kPa, respectively. The compressive strength of 20% ASF-MA$_{10\%}$ PBS hydrogel (about 75.7 kPa) was superior to that of other hydrogels
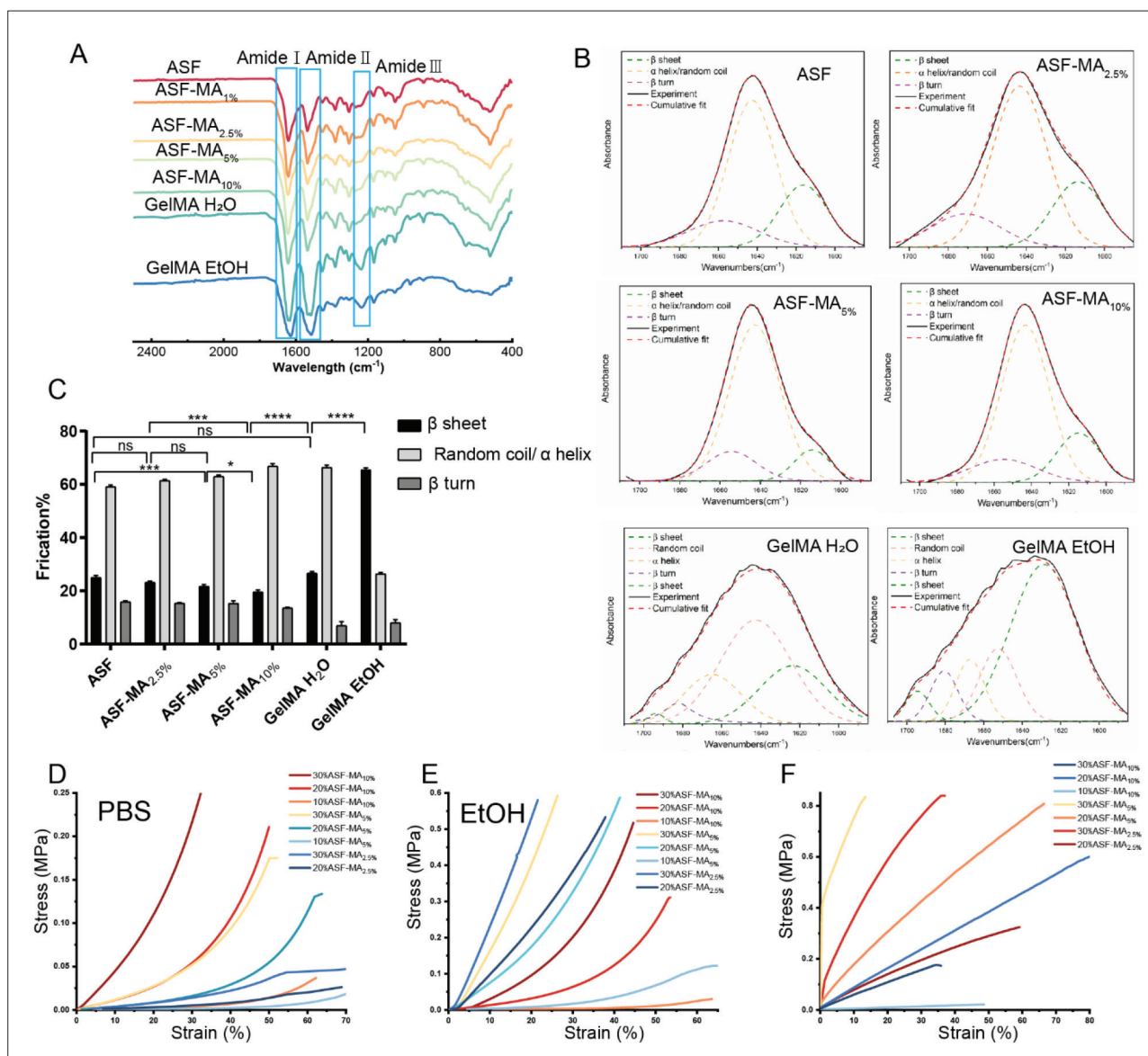
Figure 2. (A) The FTIR spectrum of ASF-MA. (B) Curve fitting analysis of ASF-MA. (C) The secondary structural fraction of ASF-MA (*ns*: $p > 0.05$, *$p < 0.05$, **$p < 0.01$, ***$p < 0.001$). (D) Compressive stress–strain curve of hydrogels immersed in PBS. (E) Compressive stress–strain curve of hydrogels immersed in 75% ethanol. (F) Tensile stress–strain curve of hydrogels soaked in 75% ethanol.

with lower methacryloylation including 30% ASF-MA$_{5\%}$ PBS hydrogel. In Figure 2E, the compressive strength of the hydrogels was almost enhanced after being soaked in 75% ethanol for 4 h. The hydrogels with the same degree of methacryloylation showed a gradual improvement in compressive strength with increasing concentration. Compared with ASF-MA$_{10\%}$ PBS hydrogel, ASF-MA$_{10\%}$ EtOH hydrogel had a smaller increment in compressive strength. The 10% ASF-MA$_{10\%}$ EtOH hydrogel was the lowest at only 6 kPa (35% deformation). For the equivalent deformation, the 20% and 30% ASF-MA$_{10\%}$ EtOH hydrogels were approximately 0.0950 and 0.298 Mpa,

which were 0.0193 and 0.0290 Mpa higher than the 20% and 30% ASF-MA$_{10\%}$ PBS hydrogels, respectively. Both low-methacryloylation ASF-MA$_{5\%}$ EtOH and ASF-MA$_{2.5\%}$ EtOH hydrogels exhibited remarkable stiffness changes. At 20% deformation, 30% ASF-MA$_{2.5\%}$ EtOH had the highest compressive modulus of 0.561 Mpa. It was 70 times more than the compressive modulus of the 30% ASF-MA$_{2.5\%}$ PBS with 0.00800 Mpa. For the compressive modulus of 30% ASF-MA$_{5\%}$ EtOH hydrogel, it was about 0.404 Mpa which was 14 times more than the compressive modulus of the 30% ASF-MA$_{5\%}$ PBS with 0.0290 Mpa. Overall, the compressive properties were generally enhanced

for the hydrogels soaked in 75% ethanol at the similar concentration and degree of methacryloylation.

There may be two main changes in the compressive properties after ethanol is treated. On the one hand, the SEM results (Figure 1D) showed that the ethanol-treated hydrogel was denser than the PBS-treated hydrogel, and it was mainly nanoporous. Simultaneously, when the concentration was higher, the material distribution of the cross-section became tighter which caused the enhancement of compression performance. On the other hand, the change of the secondary structure of ASF might be an influencing factor. By analyzing the secondary structure content, the ASF-MA$_{10\%}$ formed hydrogel which caused an increase of the β-sheet content. It also helped to enhance the compression performance, and the β-sheet content would increase sharply after soaking in ethanol. The increased β-sheet fraction implied that most of the molecules were in the crystalline state, which enhanced the hardness of hydrogel[32,33]. However, the compressive properties of the ethanol-soaked low-substituted ASF-MA hydrogels became stronger. The possible reasons might be that the small amount of MA had less effect on the ASF secondary structure, and ethanol soaking had a higher chance of β-sheet secondary structure transformation, leading to higher stiffness.

In Figure 2F, the 20% ASF-MA$_{10\%}$ EtOH hydrogel achieved the highest tensile deformation of 65%, while ASF-MA$_{5\%}$ EtOH hydrogel had stronger tensile strength. They could reach 686 kPa (54% deformation) and 830 kPa (13% deformation) at 20% and 30% concentrations, respectively. However, when the tensile strength kept at 200 kPa, 20% ASF-MA$_{2.5\%}$ EtOH hydrogel showed greater deformation, followed by 20% ASF-MA$_{10\%}$ EtOH hydrogel. It might be caused by the increased β-sheet concentration of the ethanol-treated hydrogels, which resulted in tighter structure, less susceptibility to elastic deformation, stronger stiffness, and more brittleness. Thus, 20% ASF-MA$_{10\%}$ EtOH and 20% ASF-MA$_{5\%}$ EtOH hydrogel showed better tensile deformation.

Taken together, we found that the different degrees of methacryloylation and the different solution post-treatments would have impacts on the protein secondary structure and would further affect the mechanical properties of the hydrogel. To meet the conditions of 3D bioprinting with better mechanical properties of hydrogels, we decided to choose ASF-MA$_{10\%}$ with the high degree of methacryloylation for follow-up research.

3.3. Cytocompatibility of ASF-MA
The more commonly utilized NIH/3T3 cells were used to assess the cytocompatibility of the ASF-MA$_{10\%}$ hydrogel,

while S16 cells and HUVECs were used to initially explore the delivery potential of the hydrogel for functional cells. HUVECs, which are primary cells isolated from umbilical cord veins, have a strong proliferative ability and good performance, and could be induced to form vascular structures. S16 cells are the main glial cells in the peripheral nervous system and could form myelin sheaths. S16 cells could secrete neurotrophic factors, promote the survival of damaged neurons and the regeneration of axons, and participate in the formation of nerve fibers in the peripheral nervous system. The results of the proliferation rates of the three types of cells, NIH/3T3, S16, and HUVECs, are presented in Figure 3A–C. All the three cells could proliferate normally on GelMA hydrogel, while BSF-GMA hydrogel was lack of the cell adhesion sequence RGD. Therefore, only low values were detected, and the proliferation could only be detected at day 7. However, cells could grow adherently on ASF-MA$_{10\%}$ hydrogel, and the proliferation rate was close to that on GelMA hydrogel. According to the proliferation of the three cell types on the surface of ASF-MA$_{10\%}$ PBS hydrogels and ASF-MA$_{10\%}$ EtOH hydrogels, although the cell proliferation rate was relatively slow on the ethanol-soaked hydrogels, the cells could proliferate normally.

The staining results are shown in **Figure S1 (Supplementary File)**. The NIH/3T3 cells grew in the clusters and spread all over on the GelMA hydrogel on day 5. The cell proliferation rate on ASF-MA$_{10\%}$ PBS hydrogel was faster than the rate on ASF-MA$_{10\%}$ EtOH hydrogel, which was consistent with the result of CCK-8. The cells on BSF-GMA hydrogel were not adherent on the first 3 days, and some cells gradually adapted to the new environment and started to spread around on day 5. However, when the plate was shaken vigorously, the cells could still be dislodged.

As reported, S16 cells were sensitive to the mechanical properties of the substrate materials. If the basal materials were too soft or too stiff, it would not be conducive to the spreading and growth of S16 cells[34]. We observed the cell states on four hydrogel materials. The results (Figure 3D) showed that the S16 cells grew in clusters on the GelMA hydrogel, and the cells were still able to proliferate normally. For BSF-GMA hydrogel, fewer cells were attached, but the number of proliferating cells increased significantly, which caused some single cells to spread into elongated spindle shape on day 5. For ASF-MA$_{10\%}$ hydrogel, S16 cells could spread and grow individually. For ASF-MA$_{10\%}$ PBS hydrogel, most of the S16 cells spread into elongated spindle shape, but a few cells grew in clusters on ASF-MA$_{10\%}$ EtOH hydrogel.

The growth condition of HUVECs on GelMA hydrogels was similar to that of NIH/3T3 cells (**Figure S2 in Supplementary File**). They were able to grow in
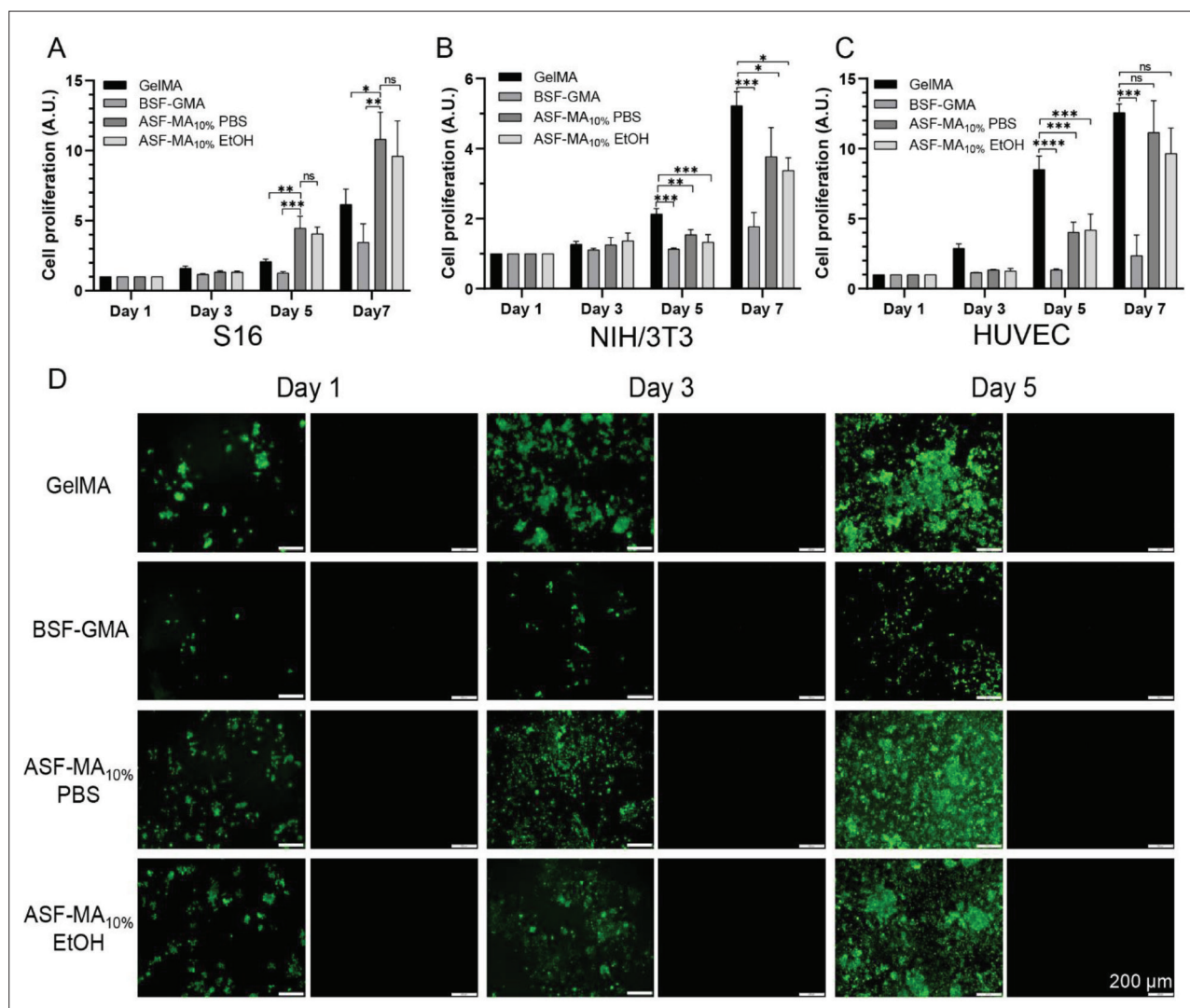
Figure 3. (A) The proliferation rate of S16 cells on various hydrogel surfaces. (B) The proliferation rate of NIH/3T3 cells on various hydrogel surfaces. (C) The proliferation rate of HUVECs on various hydrogel surfaces. (D) Fluorescence images of live/dead stained S16 cells. (*ns*: $p > 0.05$, *$p < 0.05$, **$p < 0.01$, ***$p < 0.001$)

capillary-like loops around day 3, and some dead cells were seen on day 5, which was probably due to the excessive amounts of cells. HUVECs on BSF-GMA hydrogel which grew in clumps were detached. For ASF-MA$_{10\%}$ hydrogels, HUVECs were able to grow normally, and there were almost no dead cells. Based on the results, we observed that some HUVECs could form clumps, but only a small portion of them spread and elongated under the ethanol-soaked gel condition. Under the non-ethanol-soaked hydrogel condition, HUVECs could spread better, and a few of them could form capillary-like rings.

Overall, it was concluded that the NIH/3T3, S16, and HUVECs could adhere and grow on ASF-MA$_{10\%}$ hydrogels with proper cell viability compared with BSF-GMA

hydrogels. We suspected that the HUVECs and the S16 cells under more harsh ethanol-soaked hydrogel condition grew in clumps due to their sensitivity to the mechanical properties of hydrogels. Similarly, most of the HUVECs and the S16 cells under the more gentle PBS-soaked hydrogel condition grew in individual spreads. Similarly, considering that the SEM morphology of ASF-MA H$_2$O and ASF-MA EtOH was different, we suspected that the proliferation of cells in PBS might also be related to the material morphology. 3D porous materials would be more conducive to cell adhesion and growth[35,36].

3.4. Printability of ASF-MA bioinks
To prove the 3D printability test of ASF-MA bioinks, all the printed structures were originated from designed

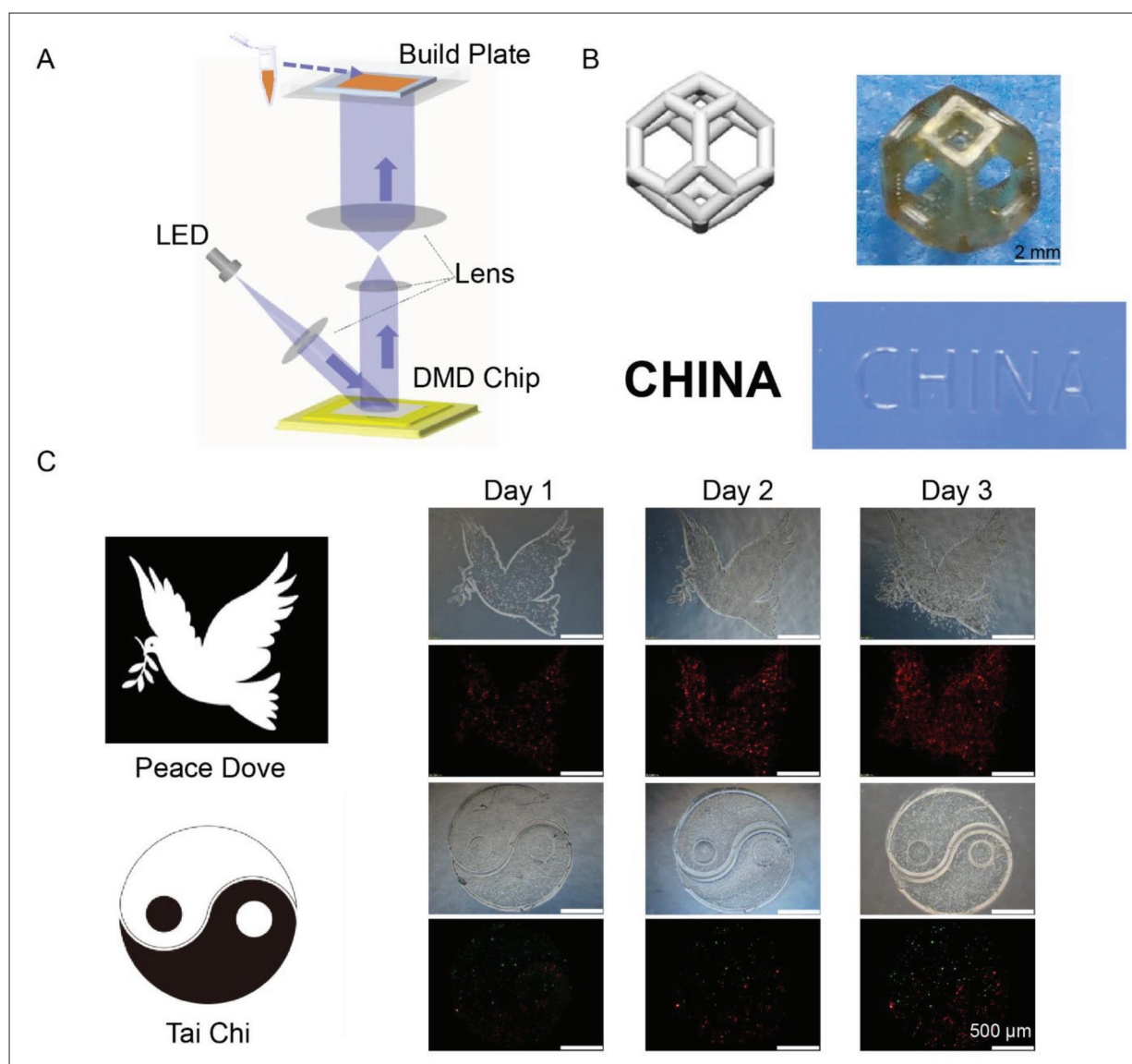**Figure 4**. (A) The system composition of the DLP 3D printer. (B) The different 3D-printed structures. (C) The 3D-bioprinted structures of the "peace dove" and the "Yin-Yang Tai Chi" diagram. The red fluorescence represented CT26-RFP RED cells, and the green fluorescence represented OP9-GFP GREEN cells.

computer-aided design (CAD) images. The principle of the continuous DLP 3D printing technology is illustrated in Figure 4A. Since ASF-MA and GelMA materials had no obvious temperature changes during the curing process, continuous 3D printing could be directly performed without lifting and cooling. By improving the system composition of the DLP 3D printer, the liquid pool that should be filled with printing ink was removed, and the printing ink was brought into between the printing plane and the sample stage through the interfacial tension of the liquid. Thus, the waste of printing ink was reduced[37-39]. Through the glass, a beam of ultraviolet light illuminates the exact cross-section of the item. The resin solidifies

as a result of the light. The item rises gradually for the resin to flow below and stay in touch with the bottom. The printing process is continuous[40]. We performed DLP 3D printing with the ASF-MA bioink, which could produce complex structures such as hollow structures and "CHINA" structures with high precision (Figure 4B). We printed fluorescent cells mixed with ASF-MA bioinks. This method could visually reflect the survival of cells inside the hydrogel. We printed the complex structure of the "peace dove " and the "Yin-Yang Tai Chi" diagram (Figure 4C). The CT26-RFP RED cells at the edge of the "peace dove" pattern had gradually grown from the inside of the hydrogel to the outside by the third day. Hydrogels
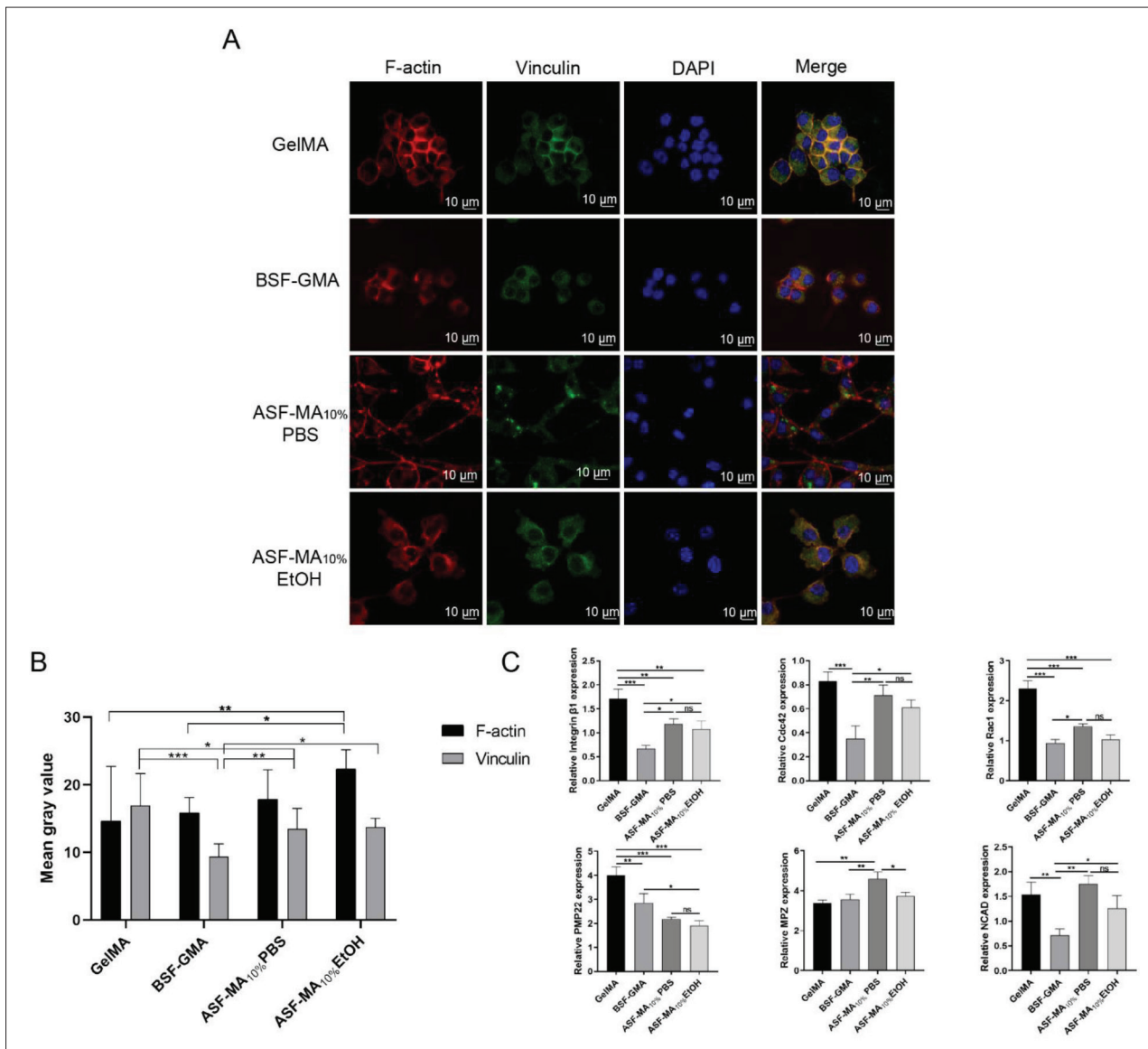
Figure 5. (A) Immunofluorescence staining images of S16 cells after being cultured on various hydrogel surfaces. The red, green, and blue fluorescence represent the cytoskeletal F-actin fibers, vinculin, and cell nuclei, respectively. (B) Semi-quantitative analysis of vinculin and F-actin fluorescence of S16 cells on the hydrogels. (C) Relative expression levels of various genes in S16 cells on various hydrogel surfaces. (*ns: $p > 0.05$, *$p < 0.05$, **$p < 0.01$, ***$p < 0.001$)

containing different types of fluorescent cells were used to print "Yin-Yang," where the hydrogel containing OP9-GFP GREEN cells represents "Yang" and the hydrogel containing CT26-RFP RED cells represents "Yin." We found that the fluorescence intensity of both cells increased on day 3. The CT26-RFP RED cells had a proper proliferation rate, while the OP9-GFP GREEN cells had a slow proliferation rate, so the intensity of red fluorescence was stronger than that of green fluorescence. According to the results, it was shown that ASF-MA could be mixed with cells for 3D printing, and the cells in the printed hydrogel could maintain a good

cell survival rate. Thus, we believed that ASF-MA bioinks had met the 3D bioprintability.

3.5. Cellular immunofluorescence

As the staining results indicated in Figure 5A, the S16 cells could spread on the ASF-MA$_{10\%}$ PBS hydrogel, with an elongated spindle shape. The nucleus was obviously oval, and the F-actin was mainly distributed at the edge of the cells with a tendency to extend outward. On the surface of the ASF-MA$_{10\%}$ EtOH hydrogel, most of the S16 cells were aggregated, and the F-actin tended to extend outward as

well. For the GelMA and BSF-GMA hydrogels, S16 cells were in a non-spreading circular state, and the F-actin was more distributed in the edge part and less distributed in the inner part of the cells. The fluorescence intensity would become higher when the cells were denser. It showed no significant difference in the average fluorescence intensity of individual cells. For vinculin, the single cell fluorescence intensity was observed under a microscope and incorporated for the fluorescence semi-quantitative analysis (Figure 5B). We noticed that a higher expression of vinculin was observed on GelMA and ASF-MA$_{10\%}$ hydrogels, and fluorescence was observed in S16 cells on ASF-MA$_{10\%}$ PBS hydrogels in some areas. In contrast, S16 cells on BSF-GMA hydrogels showed less vinculin expression and diffused fluorescence. All of the results suggested that the ASF-MA$_{10\%}$ PBS hydrogel was beneficial to the adhesion and the spreading/elongation of S16 cells, while the ASF-MA$_{10\%}$ EtOH hydrogel did not show any other obvious advantages or disadvantages.

3.6. Expression of related genes in S16 cells

S16 cells are the main glial cells in the peripheral nervous system and can form myelin sheaths. We selected several proteins related to the adhesion, motility, and myelination of S16 cells to further explore different effects of hydrogels on the growth of S16 cells. In Figure 5C, the relative expression of four genes related to cell adhesion (Integrin β1, Cdc42, Rac1, and NCAD) under the ASF-MA$_{10\%}$ PBS hydrogel condition was significantly higher than that under the BSF-GMA hydrogel condition. The expression of Integrin β1 and Rac1 under ASF-MA$_{10\%}$ PBS hydrogel condition was lower than that under GelMA hydrogel condition. Nonetheless, the expression of Cdc42 and NCAD under ASF-MA$_{10\%}$ PBS hydrogel condition was not significantly different from that under GelMA hydrogel condition. The expression of these four genes under ethanol-soaked ASF-MA$_{10\%}$ hydrogel condition was slightly lower than that under PBS-soaked hydrogel condition, but they showed no significant differences. Once again, this indicates that ASF-MA$_{10\%}$ PBS hydrogel could promote S16 cell adhesion and migration, which was comparable to that on GelMA hydrogel and significantly better than that on BSF-GMA hydrogel. The expression of the MPZ gene, which encodes a protein related to myelination, was higher on ASF-MA$_{10\%}$ PBS hydrogel compared to the other three hydrogels and showed differences. However, the expression of PMP22 gene was decreasing on GelMA, BSF-GMA, and ASF-MA$_{10\%}$ PBS hydrogels, and it gave a significant difference as a result. The S16 cell line used in our study provided the characteristics of high myelinated protein expression, and the expression of PMP22 decreased sequentially on the three hydrogels which might be due to the cell density that could affect the expression of PMP22[41-44].

For all three GelMA, BSF-GMA, and ethanol-soaked ASF-MA$_{10\%}$ hydrogels that were under the same cell density, we observed that some cells on each hydrogel grew in clusters. Thus, we came to the conclusion that the increased intercellular contact area would impact the expression of PMP22, which had less effect on MPZ protein[5,45-47]. Based on these results, it could be tentatively concluded that ASF-MA$_{10\%}$ PBS hydrogel could promote adhesion, migration, and myelination of S16 cells.

3.7. *In vitro* and *in vivo* degradation test

To evaluate the potential of hydrogels as implant materials *in vivo*, we performed *in vitro* degradation and subcutaneous implant degradation experiments on three different hydrogels. The results of *in vitro* degradation are shown in Figure 6A and B. The obviously slow degradation rate in the upper part of the figure was the hydrogel in PBS, and the faster degradation rate in the lower part was the hydrogel in PBS containing protease XIV. We could clearly see that the degradation rate of the ASF-MA PBS hydrogel was faster, and the degradation rate of the ASF-MA EtOH hydrogel was obviously slowed down, regardless of whether the hydrogel was in the PBS solution or the solution containing protease. This might be caused by increased β-sheet content and increased crystallinity[32].

As shown in Figure 6C and D, the three hydrogel materials gradually degraded under the mice's skin. The GelMA hydrogel was slightly swollen at week 1 and week 4 with 26% degradation at week 12 . The BSF-GMA hydrogel followed the similar pattern that was swollen at week 4 and then gradually degraded with 25% degradation at week 12. Compared with the GelMA hydrogel and the BSF-GMA hydrogel, ASF-MA hydrogel degraded faster with 27% at week 4. The degradation reached 32% at week 12, which was slightly higher than that of the first two hydrogels. We speculated that it might be related to the higher temperature of the regenerated ASF, which made it easier for molecular chain breakage to occur, so the ASF-MA was more susceptible to degradation.

The results of hematoxylin and eosin (H&E) section staining shown in Figure 6E suggested that the inflammatory response following the subcutaneous GelMA hydrogel implantation was weaker. At week 1, the inflammatory response was more substantial, and the outer layer of hydrogel was infiltrated with more immune cells, although it gradually weakened after 2 weeks. ASF-MA$_{10\%}$ had a weaker immune response at week 1 of implantation, which gradually became stronger afterward. By week 8, the inflammatory response gradually weakened, and some fibroblasts appeared in the outermost layer. In contrast, the inflammatory response of BSF-GMA hydrogel was more substantial and tended to diminish at week 8. While
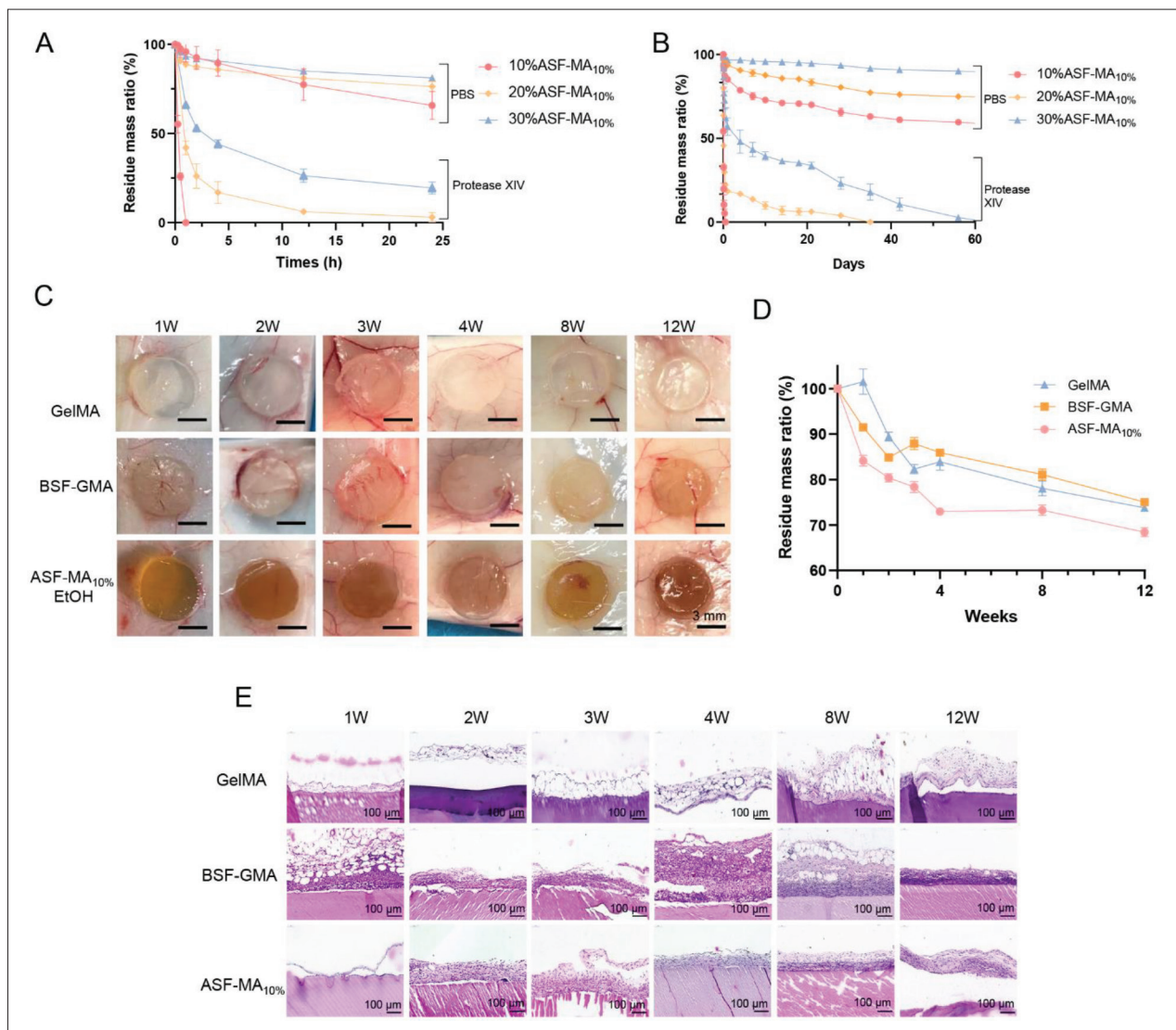
Figure 6. (A) Degradation of ASF-MA PBS hydrogels under different conditions. (B) Degradation of ASF-MA EtOH hydrogels under different conditions. (C) Hydrogels implanted into mice subcutaneously. (D) Degradation rates of different hydrogels *in vivo*. (E) H&E staining of hydrogels implanted *in vivo* at various time points.

the fibrous capsule became thicker, and the outermost layer formed fibroblasts. All three hydrogels showed an inflammatory response in the pre-implantation period in mice, which was mainly caused by foreign body immune rejection when the pore size of the implanted material also affected the inflammatory response[44-46].

When the pore size became smaller, the cell migration rate and cell infiltration rate would be slow. As a result, we could see the enhancement of the inflammation. After 2 months, the inflammation resolved on all three hydrogels, and the gradual formation of fibroblasts occurred. In summary, ASF-MA$_{10\%}$ EtOH hydrogel had relatively better biocompatibility. Genetic engineering of

ASF should be considered in future studies to optimize the molecular structure design. In addition, mixing with other biomaterials based on the demand and expanding the testing on other types of animals are also warranted.

4. Discussion

3D-printed biomaterials for tissue engineering are essential in the repair of tissue and organ defect and in the regenerative reconstruction research. The 3D-printed biomaterials should have the attributes of printability, biocompatibility, mechanical properties, and degradability so as to provide a bionic environment with both exogenous and endogenous cells similar to the extracellular matrix.

DLP 3D printing technology has been widely used in tissue engineering due to its high precision and fast molding speed. However, the functional biological materials were limited because the printing ink still needs to meet the characteristics of the photopolymerization reaction. BSF has been explored for biomedical applications since the last century because it is easily accessible,[48] and it has promoted the development of silk fibroin with RGD sequences. The researchers added crosslinking agents to BSF to create porous scaffolds materials, such as glutaraldehyde[49], EDC, and NHS[50]. For example, Park *et al.* used GMA-modified silk fibroin for DLP 3D printing. It showed great printability and could be mixed with chondrocytes to produce artificial tracheal scaffolds for *in vivo* use[6]. The result from Park *et al.* prompted us to try to modify the functional groups of regenerated ASF. In the current study, methacrylic anhydride was reacted with free amino groups to introduce photopolymerizable methacryloyl groups into the molecular chain of ASF, which produced the modified molecular with photopolymerization properties. However, significant difference existed between ASF's primary amino acid composition and BSF composed mainly of glycine-alanine-glycine-serine-glycine-alanine (GAGSGA) repeats[51]. At the same time, the hydrophobic amino acids alanine (43.07%) and glycine (27.27%) in ASF were higher and contained more repetitive sequences of alanine. The MA was also hydrophobic. Therefore, when the reaction between MA and the amino group exceeded a certain level, the ASF would become hydrophobic and unstable in an aqueous solution leading to precipitation. Based on the ^{1}H-NMR and FTIR spectra, the content of the secondary structure β-fold of ASF decreased slightly with the increase of the degree of methacryloylation. It might be one of the reasons causing the instability. In the present study, a high methacrylate-substitution level of 45.98% (ASF-MA$_{10\%}$) was achieved by repeating the preparation process.

As the accuracy of printing is a significant factor for the personalized 3D-printed products and the precise medical treatment, a DLP 3D printer with high printing accuracy was used in our study. The physicochemical properties of the printing ink, such as like photoreaction rate and light transmission, also affected the accuracy of the printed structures. The ASF-MA$_{10\%}$ bioinks obtained formed hydrogel after exposure to 405 nm UV light with 80 mW/cm^2 intensity for 5 s. It could print complex 3D hollow structures with printability after adding 0.1% lemon yellow to reduce other light interferences. On the other hand, the bioink prepared with mixing ASF-MA$_{10\%}$ with cells enabled the printing of specific structures. The viability of cells within the ASF-MA hydrogel remained at a good level, compared with some synthetic materials,

such as PEGDA, polyurethane, and poly (glycerol sebacate methacrylate)[5,52]. Thus, ASF-MA hydrogels have potential application prospects in 3D printing cell delivery system.

Another important factor to consider in printing 3D tissue structures is the mechanical properties, which also influence the functioning of cells and tissues[53]. Collagen and hyaluronic acid are both components of the extracellular matrix and have great biocompatibility. However, the compressive strength was generally at 10–100 kPa and had inferior tensile performance. As for PEGDA and BSF-GMA, they showed superior compressive modulus of about 1 MPa, but the difficulty of cell adhesion on the hydrogels affected the normal function of cells and tissues to some extents. In our study, the mechanical properties of hydrogels under different conditions were explored. We observed that 30% ASF-MA$_{10\%}$ PBS hydrogel had the highest compressive modulus of 0.269 MPa (at 35% deformation), and it was better than BSF-GMA and GelMA hydrogels of the same concentration. In addition, the mechanical properties of the 75% ethanol-soaked ASF-MA hydrogels were all improved due to the change of the secondary structure and hydrophobic network structure. At the 20% deformation, 30% ASF-MA$_{2.5\%}$ EtOH hydrogels could be compressed with a modulus of 0.561 MPa. At the 13% deformation, 30% ASF-MA$_{5\%}$ EtOH hydrogels possessed a maximum tensile modulus of about 0.830 MPa. Based on the approximate elastic modulus of human tissues[53], the different ASF-MA hydrogels fabricated in our study exhibited varying mechanical properties which could potentially be applied in constructing tissues and organs, such as skin, liver, and kidney.

Biodegradability is also an significant characteristic of tissue engineering materials. Under ideal condition, the bionic structure should degrade slowly while the new tissue gradually grows. At the same time, the degraded products should not cause side effects to the organism[54]. Gelatin, collagen, elastin, and silk fibroin are natural protein materials, and most of the degradation products were non-toxic, such as amino acids and short peptides, which are favorably biocompatible[6]. According to our study, the ASF-MA$_{10\%}$ PBS hydrogel degraded rapidly in the presence of protease XIV. However, the ASF-MA EtOH hydrogel degraded more slowly in the protease-containing environment due to the increased crystallinity. The *in vivo* experiments showed that ASF-MA$_{10\%}$ hydrogel degraded by about 30% in 3 months after implantation into mice, with a rate slightly higher than that of GelMA and BSF-GMA hydrogels, and did not manifest swelling. Therefore, our study provided a selection of ASF-MA hydrogels with different degradation rates for 3D printing, and it could

meet the requirements of different tissue and organ defect repair and regeneration with different degradation rates.

Compared with some hydrogels without RGD sequence, such as BSF-GMA, PEGDA, and sodium alginate, ASF required no additional modifications or corresponding sequences since it has its own RGD sequence. In our study, ASF-MA$_{10\%}$ hydrogel showed great cell adhesion. NIH/3T3, S16, and HUVECs multiplied normally after the inoculation on the surface. The ASF-Ma EtOH hydrogels presented no significant advantage for cell proliferation, but we observed subtle differences in cell morphology and migration. Previous studies have indicated that S16 cells and HUVECs were sensitive to the properties of substrate material. HUVECs aggregated more easily on softer hydrogels (E ≈ 2 kPa) and developed capillary-like loops prematurely, while on harder hydrogels (E ≈ 15 kPa), they were less likely to aggregate and the formation of loops was delayed[55]. Their proliferation rate decreased remarkably on rigid hydrogels[56]. Similarly, S16 cells were sensitive to the matrix material. It showed a tendency for bipolar elongation on the laminin-coated basal material (E ≈ 20 kPa) and had a multipolar morphology on the same basal material with E ≈ 1 kPa[57]. The surface morphology of the substrates also contributed to the morphology and migration of S16 cells[58,59]. In our study, HUVECs and S16 cells showed biological effects similar to those reported in previous studies. According to the sequence of hydrogel compression properties, i.e., ASF-MA$_{10\%}$ EtOH > ASF-MA$_{10\%}$ PBS > GelMA > BSF-GMA, S16 cells showed significant spreading/elongation on 20% ASF-MA$_{10\%}$ PBS hydrogel. The relative expression of S16 cell adhesion-, migration-, and myelination-related genes was slightly higher. Preliminarily, the results suggested that ASF-MA$_{10\%}$ PBS hydrogel may promote the migratory movement of S16 cells, but the specific molecular mechanisms, including the molecular pathways and upstream and downstream regulatory proteins, are still not clear. Currently, delineation of the crucial functions of 3D-printed scaffold materials in peripheral nerve repair is still underway. Our next goal is to work on the repair of peripheral nerve defect. We shall also focus on the physicochemical and biological properties of ASF-MA hydrogels to confirm the feasibility of ASF-MA as a scaffold material for other tissue engineering applications in different tissues and organs, such as skin, blood vessels, and kidneys.

5. Conclusion

We synthesized ASF-MA for photocured 3D bioprinting by modifying ASF molecular chains chemically with a preparation process and printing performance. The compressive and tensile properties of ASF-MA hydrogel were improved with 75% ethanol immersion. In addition, ASF-MA hydrogels provided biocompatibility and biological functions to promote the adhesion, migration, and proliferation of S16 cells compared to other types of hydrogels. At the same time, the cell-loaded tissue constructs had a favorable cell survival rate. Therefore, ASF-MA can be used for 3D printing such as DLP and has the potential applications in biomedical fields.

Conflict of interest

The authors declare no conflict of interest.

Author contributions

Conceptualization: Yulan Huang, Xue Zhang
Data curation: Xue Zhang, Yulan Huang
Investigation: Xue Zhang, Yulan Huang, Xiong Yang
Methodology: Wenbi Wu, Yulan Huang, Xue Zhang
Project administration: Maling Gou
Writing – original draft: Xue Zhang
Writing – review & editing: Maling Gou, Xue Zhang, Wenbi Wu

Ethics approval and consent to participate

All animal experiments were approved by the Experimental Animal Ethics Committee of West China Hospital of Sichuan University (ethics approval number 2020370A) and conducted in accordance with the Guide for the Care and Use of Laboratory Animals.

Consent for publication

Not applicable.

Availability of data

The data of this study are available from the corresponding author upon reasonable request.

References

1. Yao X, Zou S, Fan S, *et al.*, 2022, Bioinspired silk fibroin materials: From silk building blocks extraction and reconstruction to advanced biomedical applications. *Mater Today Bio*, 16: 100381.

   https://doi.org/10.1016/j.mtbio.2022.100381

2. Hu Y, Lee A, Chang S, *et al.*, 2022, Biomaterial-induced conversion of quiescent cardiomyocytes into pacemaker cells in rats. *Nat Biomed Eng*, 6(4): 421–434.

   https://doi.org/10.1038/s41551-021-00812-y

3. Grigoryan B, Paulsen SJ, Corbett DC, *et al.*, 2019, Multivascular networks and functional intravascular topologies within biocompatible hydrogels. *Science*, 364(6439): 458–464.

   https://doi.org/10.1126/science.aav9750

4. Lee A, Hudson AR, Shiwarski DJ, *et al.*, 2019, 3D bioprinting of collagen to rebuild components of the human heart. *Science*, 365(6452): 482–487.

   https://doi.org/10.1126/science.aav9051

5. Yu C, Schimelman J, Wang P, *et al.*, 2020, Photopolymerizable biomaterials and light-based 3D printing strategies for biomedical applications. *Chem Rev*, 120(19): 10695–10743.

   https://doi.org/10.1021/acs.chemrev.9b00810

6. Unagolla JM, Jayasuriya AC, 2020, Hydrogel-based 3D bioprinting: A comprehensive review on cell-laden hydrogels, bioink formulations, and future perspectives. *Appl Mater Today*, 18: 100479.

   https://doi.org/10.1016/j.apmt.2019.100479

7. Kim SH, Hong H, Ajiteru O, *et al.*, 2021, 3D bioprinted silk fibroin hydrogels for tissue engineering. *Nat Protoc*, 16(12): 5484–5532.

   https://doi.org/10.1038/s41596-021-00622-1

8. Hong H, Seo YB, Kim DY, *et al.*, 2020, Digital light processing 3D printed silk fibroin hydrogel for cartilage tissue engineering. *Biomaterials*, 232:119679.

   https://doi.org/10.1016/j.biomaterials.2019.119679

9. Lee YJ, Lee JS, Ajiteru O, *et al.*, 2022, Biocompatible fluorescent silk fibroin bioink for digital light processing 3D printing. *Int J Biol Macromol*, 213:317–327.

   https://doi.org/10.1016/j.ijbiomac.2022.05.123

10. Wu X, Zhou M, Jiang F, *et al.*, 2021, Marginal sealing around integral bilayer scaffolds for repairing osteochondral defects based on photocurable silk hydrogels. *Bioact Mater*, 6(11): 3976–3986.

    https://doi.org/10.1016/j.bioactmat.2021.04.005

11. Zou S, Yao X, Shao H, *et al.*, 2022, Nonmulberry silk fibroin-based biomaterials: Impact on cell behavior regulation and tissue regeneration. *Acta Biomater*, 153: 68–84.

    https://doi.org/10.1016/j.actbio.2022.09.021

12. Tang X, Chen X, Zhang S, *et al.*, 2021, Silk-inspired in situ hydrogel with anti-tumor immunity enhanced photodynamic therapy for melanoma and infected wound healing. *Adv Funct Mater*, 31(17): 2101320.

    https://doi.org/10.1002/adfm.202101320

13. Naskar D, Sapru S, Ghosh AK, *et al.*, 2021, Nonmulberry silk proteins: Multipurpose ingredient in bio-functional assembly. *Biomed Mater*, 16(6): 062002.

    https://doi.org/10.1088/1748-605X/ac20a0

14. Ma Y, Duan L, Sun J, *et al.*, 2022, Oral nanotherapeutics based on Antheraea pernyi silk fibroin for synergistic treatment of ulcerative colitis. *Biomaterials*, 282: 121410.

    https://doi.org/10.1016/j.biomaterials.2022.121410

15. Kim SH, Yeon YK, Lee JM, *et al.*, 2018, Precisely printable and biocompatible silk fibroin bioink for digital light processing 3D printing. *Nat Commun*, 9(1): 1620.

    https://doi.org/10.1038/s41467-018-03759-y

16. Li X, Zhang Q, Ye D, *et al.*, 2017, Fabrication and characterization of electrospun PCL/Antheraea pernyi silk fibroin nanofibrous scaffolds. *Polym Eng Sci,* 57(2): 206–213.

    https://doi.org/10.1002/pen.24402

17. Lee K, Kweon H, Yeo J, *et al.*, 2011, Characterization of tyrosine-rich Antheraea pernyi silk fibroin hydrolysate. *Int J Biol Macromol*, 48(1): 223–226.

    https://doi.org/10.1016/j.ijbiomac.2010.09.020

18. Guan J, Zhu W, Liu B, *et al.*, 2017, Comparing the microstructure and mechanical properties of Bombyx mori and Antheraea pernyi cocoon composites. *Acta Biomater*, 47: 60–70.

    https://doi.org/10.1016/j.actbio.2016.09.042

19. Yang K, Guan J, Numata K, *et al.*, 2019, Integrating tough Antheraea pernyi silk and strong carbon fibres for impact-critical structural composites. *Nat Commun*, 10(1): 3786.

    https://doi.org/10.1038/s41467-019-11520-2

20. Wang J, Chen Y, Zhou G, *et al.*, 2019, Polydopamine-coated Antheraea pernyi (A. pernyi) silk fibroin films promote cell adhesion and wound healing in skin tissue repair. *ACS Appl Mater Interfaces*, 11(38): 34736–34743.

    https://doi.org/10.1021/acsami.9b12643

21. Wang J, Yin Z, Xue X, *et al.*, 2016, Natural non-mulberry silk nanoparticles for potential-controlled drug release. *Int J Mol Sci*, 17(12): 2012.

    https://doi.org/10.3390/ijms17122012

22. Cui B, Zhang C, Gan B, *et al.*, 2020, Collagen-tussah silk fibroin hybrid scaffolds loaded with bone mesenchymal stem cells promote skin wound repair in rats. *Mater Sci Eng C*, 109: 110611.

https://doi.org/10.1016/j.msec.2019.110611

23. Zou S, Wang X, Fan S, *et al.*, 2019, Fabrication and characterization of regenerated Antheraea pernyi silk fibroin scaffolds for Schwann cell culturing. *Eur Polym J*, 117: 123–133.

https://doi.org/10.1016/j.eurpolymj.2019.04.056

24. Yan S, Zhao C, Wu X, *et al.*, 2010, Gelation behavior of Antheraea pernyi silk fibroin. *Sci China Chem*, 53(3): 535–541.

https://doi.org/10.1007/s11426-010-0093-0

25. Lee BH, Lum N, Seow LY, *et al.*, 2016, Synthesis and characterization of types A and B gelatin methacryloyl for bioink applications. *Materials*, 9(10): 797.

https://doi.org/10.3390/ma9100797

26. Carbonaro M, Nucara A, 2010, Secondary structure of food proteins by Fourier transform spectroscopy in the mid-infrared region. *Amino Acids*, 38(3): 679–690.

https://doi.org/10.1007/s00726-009-0274-3

27. Taddei P, Tsukada M,Freddi G, 2013, Affinity of protein fibres towards sulfation. *J Raman Spectrosc*, 44(2): 190–197.

https://doi.org/10.1002/jrs.4168

28. Shirahama H, Lee BH, Tan LP, *et al.*, 2016, Precise tuning of facile one-pot gelatin methacryloyl (GelMA) synthesis. *Sci Rep*, 6(1): 31036.

https://doi.org/10.1038/srep31036

29. Kumar M, Gupta P, Bhattacharjee S, *et al.*, 2018, Immunomodulatory injectable silk hydrogels maintaining functional islets and promoting anti-inflammatory M2 macrophage polarization. *Biomaterials*, 187: 1–17.

https://doi.org/10.1016/j.biomaterials.2018.09.037

30. Li XF, Zhang J, Feng YF, *et al.*, 2018, Tuning the structure and performance of silk biomaterials by combining mulberry and non-mulberry silk fibroin. *Polym Degrad Stab*, 147: 57–63.

https://doi.org/10.1016/j.polymdegradstab.2017.11.013

31. Slaughter BV, Khurshid SS, Fisher OZ, *et al.*, 2009, Hydrogels in regenerative medicine. *Adv Mater*, 21(32–33): 3307–3329.

https://doi.org/10.1002/adma.200802106

32. Xiao WQ, He JK, Nichol JW, *et al.*, 2011, Synthesis and characterization of photocrosslinkable gelatin and silk fibroin interpenetrating polymer network hydrogels. *Acta Biomater*, 7(6): 2384–2393.

https://doi.org/10.1016/j.actbio.2011.01.016

33. Dadras Chomachayi M, Solouk A, Mirzadeh H, 2019, Improvement of the electrospinnability of silk fibroin solution by atmospheric pressure plasma treatment. *Fibers Polym*, 20(8): 1594–1600.

https://doi.org/10.1007/s12221-019-9015-8

34. Gu Y, Ji Y, Zhao Y, *et al.*, 2012, The influence of substrate stiffness on the behavior and functions of Schwann cells in culture. *Biomaterials*, 33(28): 6672–6681.

https://doi.org/10.1016/j.biomaterials.2012.06.006

35. Xu Y, Gu Y, Cai F, *et al.*, 2020, Metabolism balance regulation via antagonist-functionalized injectable microsphere for nucleus pulposus regeneration. *Adv Funct Mater*, 30(52): 2006333.

https://doi.org/10.1002/adfm.202006333

36. Sun J, Li J, Huan Z, *et al.*, 2023, Mesenchymal stem cell-laden composite β cell porous microgel for diabetes treatment. *Adv Funct Mater*, 2211897.

https://doi.org/10.1002/adfm.202211897

37. Hu Y, Zhang Q, You R, *et al.*, 2012, The relationship between secondary structure and biodegradation behavior of silk fibroin scaffolds. *Adv Mater Sci Eng*, 2012: 185905.

https://doi.org/10.1155/2012/185905

38. Tao J, Zhang J, Du T, *et al.*, 2019, Rapid 3D printing of functional nanoparticle-enhanced conduits for effective nerve repair. *Acta Biomater*, 90: 49–59.

https://doi.org/10.1016/j.actbio.2019.03.047

39. Xu X, Tao J, Wang S, *et al.*, 2019, 3D printing of nerve conduits with nanoparticle-encapsulated RGFP966. *Appl Mater Today*, 16: 247–256.

https://doi.org/10.1016/j.apmt.2019.05.014

40. Dendukuri D, Pregibon DC, Collins J, *et al.*, 2006, Continuous-flow lithography for high-throughput microparticle synthesis. *Nat Mater*, 5(5): 365–369.

https://doi.org/10.1038/nmat1617

41. DUrso D, Ehrhardt P, Müller HW, 1999, Peripheral myelin protein 22 and protein zero: A novel association in peripheral nervous system myelin. *J Neurosci*, 19(9): 3396.

https://doi.org/10.1523/JNEUROSCI.19-09-03396.1999

42. Sasagasako N, Toda K, Hollis M, *et al.*, 1996, Myelin gene expression in immortalized schwann cells: Relationship to cell density and proliferation. *J Neurochem*, 66(4): 1432–1439.

https://doi.org/10.1046/j.1471-4159.1996.66041432.x

43. Sasagasako N, Ohno M,Quarles RH, 1999, Evidence for regulation of myelin protein synthesis by contact between adjacent schwann cell plasma membranes. *Dev Neurosci*, 21(6): 417–422.

https://doi.org/10.1159/000017409

44. Li G, Zhao X, Zhang L, *et al.*, 2020, Anisotropic ridge/groove microstructure for regulating morphology and biological function of Schwann cells. *Appl Mater Today*, 18: 100468.

https://doi.org/10.1016/j.apmt.2019.100468

45. Tylek T, Blum C, Hrynevich A, *et al.*, 2020, Precisely defined fiber scaffolds with 40 μm porosity induce elongation driven M2-like polarization of human macrophages. *Biofabrication*, 12(2): 025007.

https://doi.org/10.1088/1758-5090/ab5f4e

46. Dai Y, Li X, Wu R, *et al.*, 2018, Macrophages of different phenotypes influence the migration of BMSCs in PLGA scaffolds with different pore size. *Biotechnol J*, 13(1): 1700297.

https://doi.org/10.1002/biot.201700297

47. Song E, Yeon Kim S, Chun T, *et al.*, 2006, Collagen scaffolds derived from a marine source and their biocompatibility. *Biomaterials*, 27(15): 2951–2961.

https://doi.org/10.1016/j.biomaterials.2006.01.015

48. Altman GH, Diaz F, Jakuba C, *et al.*, 2003, Silk-based biomaterials. *Biomaterials*, 24(3): 401–416.

https://doi.org/10.1016/S0142-9612(02)00353-8

49. Xie H, Gu Z, Li C, *et al.*, 2016, A novel bioceramic scaffold integrating silk fibroin in calcium polyphosphate for bone tissue-engineering. *Ceram Int*, 42(2, Part A): 2386–2392.

https://doi.org/10.1016/j.ceramint.2015.10.036

50. You R, Xu Y, Liu Y, *et al.*, 2015, Comparison of the in vitro and in vivo degradations of silk fibroin scaffolds from mulberry and nonmulberry silkworms. *Biomed Mater*, 10(1): 015003.

https://doi.org/10.1088/1748-6041/10/1/015003

51. Guo C, Zhang J, Jordan JS, *et al.*, 2018, Structural comparison of various silkworm silks: An insight into the structure–property relationship. *Biomacromolecules*, 19(3): 906–917.

https://doi.org/10.1021/acs.biomac.7b01687

52. Singh D, Harding AJ, Albadawi E, *et al.*, 2018, Additive manufactured biodegradable poly(glycerol sebacate methacrylate) nerve guidance conduits. *Acta Biomater*, 78: 48–63.

https://doi.org/10.1016/j.actbio.2018.07.055

53. Guimarães CF, Gasperini L, Marques AP, *et al.*, 2020, The stiffness of living tissues and its implications for tissue engineering. *Nat Rev Mater*, 5(5): 351–370.

https://doi.org/10.1038/s41578-019-0169-1

54. Guvendiren M, Molde J, Soares RMD, *et al.*, 2016, Designing biomaterials for 3D printing. *ACS Biomater Sci Eng*, 2(10): 1679–1693.

https://doi.org/10.1021/acsbiomaterials.6b00121

55. Kim S, Kawai T, Wang D, *et al.*, 2016, Engineering a dual-layer chitosan–lactide hydrogel to create endothelial cell aggregate-induced microvascular networks in vitro and increase blood perfusion in vivo. *ACS Appl Mater Interfaces*, 8(30): 19245–19255.

https://doi.org/10.1021/acsami.6b04431

56. Pandit V, Zuidema JM, Venuto KN, *et al.*, 2013, Evaluation of multifunctional polysaccharide hydrogels with varying stiffness for bone tissue engineering. *Tissue Eng Part A*, 19(21–22): 2452–2463.

https://doi.org/10.1089/ten.tea.2012.0644

57. Rosso G, Liashkovich I, Young P, *et al.*, 2017, Schwann cells and neurite outgrowth from embryonic dorsal root ganglions are highly mechanosensitive. *Nanomedicine*, 13(2): 493–501.

https://doi.org/10.1016/j.nano.2016.06.011

58. Wu Y-X, Ma H, Wang J-L, *et al.*, 2021, Production of chitosan scaffolds by lyophilization or electrospinning: Which is better for peripheral nerve regeneration? *Neural Regen Res*, 16(6): 1093–1098.

https://doi.org/10.4103/1673-5374.300463

59. Naghilou A, Pöttschacher L, Millesi F, *et al.*, 2020, Correlating the secondary protein structure of natural spider silk with its guiding properties for Schwann cells. *Mater Sci Eng C*, 116: 111219.

https://doi.org/10.1016/j.msec.2020.111219